Simulation of 3D concrete printing using an implicit formulation of the moving particle semi-implicit method

Daniela dos Santos da Mata Gomes[1], Melina Rocutan[1], Lucas Soares Pereira[1], Fabio Kenji Motezuki[1], Liang-Yee Cheng[1]

[1] *Department of Construction Engineering, University of São Paulo*
Av. Prof. Almeida Prado, 83 - Butantã, 05508-070, São Paulo - SP, Brazil
daniela_gomes@usp.br, rocutanmelina@usp.br, lucas_pereira@usp.br, fmote@usp.br, cheng.yee@usp.br

Abstract. Additive construction techniques, such as 3D Concrete Printing (3DCP), offer significant advantages, including reduced material waste, optimized construction times, and the ability to create complex shapes. Despite advancements, predicting printing results remains challenging. Fresh material properties are crucial, making numerical modeling essential for investigating the dynamic aspects of the extrusion process. However, modeling 3DCP is challenging due to the complex rheological behavior of self-supporting concrete, which exhibits high yield stress and high apparent viscosity at low deformation rates. To address these challenges, the Moving Particle Semi-Implicit (MPS) method was adopted in the present study to model the flow. Conventional MPS has numerical restrictions with highly viscous fluids, requiring very small time steps and resulting in huge processing costs. This study uses an implicit algorithm allowing for larger time steps and reduced processing time. Simulations of non-Newtonian flow between parallel plates were validated using analytical solutions. 3DCP simulations described the flow of fresh mortar at different printing speeds and extrusion volumetric fluxes. The cross-sectional shapes of extruded layers compared with experimental data showed qualitative agreement, demonstrating the potential of the implicit MPS method for modeling 3DCP processes.

Keywords: 3D concrete printing; non-Newtonian fluid; moving particle semi-implicit (MPS).

1 Introduction

Non-Newtonian flows have many applications in industries like food, civil, and petroleum engineering. The challenge lies in understanding their rheology to predict their dynamic behavior accurately. This is especially important for 3D Concrete Printing (3DCP), a Material Extrusion-based Additive Manufacturing (AM) technique that reduces waste, time, and cost while enhancing design flexibility by allowing the creation of complex, customized components used for large-scale projects like walls and facades [1,2].

3DCP works by extruding concrete through a nozzle to form shapes controlled by a printer or robotic arm. This scalable method depends on material properties and rheology [3–6]. The characteristics of the flow in this context are incompressible, highly viscous, and free surface. However, current simulation tools are still developing, presenting challenges in predicting outcomes [7]. Effective modeling must consider material properties, rheology, and dynamic conditions [8,9].

This study aims to enhance the understanding of the non-Newtonian fluid behavior in 3DCP using a Lagrangian modeling approach. For this purpose, the moving particle semi-implicit (MPS) method will be employed to model the incompressible, highly viscous and deformable free-surface non-Newtonian fluid flows. MPS's focus on incompressibility ensures more precise simulations of the concrete extrusion process.

2 Numerical modeling

The numerical method employed in this study is based on the Moving Particle Semi-Implicit (MPS) approach, first introduced by Koshizuka & Oka [10] for modeling incompressible free-surface flows.

2.1 Governing equations

For incompressible flows, using the Lagrangian description, the Navier-Stokes equations of conservation of mass and momentum are given, respectively, by:

$$\frac{D\rho}{Dt} = -\rho \nabla \cdot \mathbf{u} = 0. \tag{1}$$

$$\frac{D\mathbf{u}}{Dt} = \frac{1}{\rho} \left(-\nabla P + \nabla \cdot \mathbb{T} \right) + \mathbf{f}. \tag{2}$$

where ρ is the fluid density, t is time, $\mathbf{u}$ is the velocity vector, P is pressure; $\mathbb{T}$ is the stress tensor, and $\mathbf{f}$ is the vector representing external forces.

In the momentum conservation equation, the representation of the viscous term is given by the divergence of the viscous stress tensor, $\nabla \cdot \mathbb{T}$, where the viscous stress tensor is given by:

$$\mathbb{T} = 2\eta \mathbb{D}. \tag{3}$$

where η is the apparent viscosity and $\mathbb{D}$ is the rate of strain tensor, given by:

$$\eta = \frac{\tau}{\dot{\gamma}}. \tag{4}$$

$$\mathbb{D} = \frac{1}{2} \left[(\nabla \mathbf{u}) + (\nabla \mathbf{u})^{\mathbf{T}} \right]. \tag{5}$$

where τ is the shear stress and $\dot{\gamma}$ is the strain rate.

The strain rate $\dot{\gamma}$, for a simple Newtonian fluid, can be expressed as:

$$\dot{\gamma} = \sqrt{2\mathbb{D} : \mathbb{D}}. \tag{6}$$

where $\mathbb{D} : \mathbb{D}$ represents the product of the tensor $\mathbb{D}$. Substituting equation (5) into the above expression, we have:

$$\dot{\gamma} = \sqrt{\frac{1}{2} \left[(\nabla \mathbf{u}) + (\nabla \mathbf{u})^{T} \right] : \left[(\nabla \mathbf{u}) + (\nabla \mathbf{u})^{T} \right]}. \tag{7}$$

Thus, the strain rate $\dot{\gamma}$ is directly related to the velocity gradient $\nabla \mathbf{u}$ of the fluid, and the divergence of the stress tensor $(\nabla \cdot \mathbb{T})$ can be expressed as:

$$\nabla \cdot \mathbb{T} = 2\mathbb{D} \cdot \nabla \eta + \eta \nabla^2 \mathbf{u}. \tag{8}$$

2.2 Bingham-Papanastasius Model

Non-Newtonian fluids have a nonlinear relationship between shear stress and deformation rate. Different constitutive equations describe these fluids, depending on the fluid type. The Bingham model is one of the well-known rheological models. This model has a minimum shear stress, called yield stress, that must be exceeded for the fluid to flow. The constitutive equation for Bingham fluids is:

$$\begin{cases} \tau = \tau_0 + \mu_p \dot{\gamma}, & |\tau| \geq \tau_0 \\ \dot{\gamma} = 0, & |\tau| < \tau_0 \end{cases}. \tag{9}$$

where τ_0 is the yield stress and μ_p is the plastic viscosity.

If $\tau < \tau_0$, the fluid does not flow, leading to infinite viscosity. This model also shows a break in the deformation field when the stress equals τ_0.

To overcome this problem, Papanastasiou [11] introduced an equation to regularize viscoplastic functions.

This equation uses a regularization parameter m to create continuous shear stress and viscoplastic viscosity functions, applicable to both fluid and solid regions.

2.3 Moving Particle semi-implicit method

In the MPS method, spatial differential operators are approximated with discrete differential operators o irregular nodes. These are based on a weight function W_{ij} that shows the influence of a neighboring particle j on a particle i. The weight function originally proposed by Koshizuka & Oka [10] is:

$$W_{ij} = \begin{cases} \frac{r_e}{\|\mathbf{r}_{ij}\|} - 1, & \|\mathbf{r}_{ij}\| \leq r_e \\ 0 & , \quad \|\mathbf{r}_{ij}\| > r_e \end{cases}. \tag{10}$$

where r_e is the effective radius that limits the radius of influence and $\|\mathbf{r}_{ij}\| = \|\mathbf{r}_j - \mathbf{r}_i\|$ is the distance between particles i and j (Figure 1).
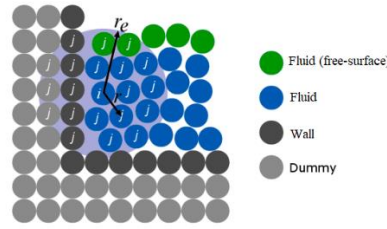
Figure 1: Representation of neighboring particles j within the influence region of radius r_e around a particle i.

The original MPS method uses a semi-implicit algorithm to solve the flow equations by splitting each time step into predictive and corrective stages. The velocity and position of a fluid particle i are predicted explicitly using the diffusion terms and external forces from the momentum conservation equation. The formulation is as follows:

$$\mathbf{u}_i^* = \mathbf{u}_i^t + \frac{\Delta t}{\rho}[\eta\langle\nabla^2 \mathbf{u}\rangle_i + \rho\mathbf{f}]^t. \tag{11}$$

$$\mathbf{r}_i^* = \mathbf{r}_i^t + \Delta t\mathbf{u}_i^*. \tag{12}$$

where the superscript* refers to the predictive stage.

The pressure at fluid and wall particles is calculated by solving a linear system using the pressure Poisson equation (PPE). This study uses the Time-scale Correction of Particle-level Impulses (TCPI) source term proposed by Cheng et al. [12].

$$\langle\nabla^2 P\rangle_i^{t+\Delta t} - \frac{\rho}{\Delta t^2}\alpha_c P_i^{t+\Delta t} = C_s^2 \frac{\rho}{l_0^2} \frac{pnd^0 - pnd_i^t}{pnd^0} + C_s \frac{\rho}{l_0}\langle\nabla \cdot \mathbf{u}^{**}\rangle_i \tag{13}$$

Here, pnd_i^t is the number density of particle i at the start of time t, α_c is the artificial compressibility coefficient, and C_s is the speed at which perturbations spread. The velocity of fluid particles $\mathbf{u}_i^{t+\Delta t}$ is updated using the pressure gradient term from momentum conservation, and the new positions $\mathbf{r}_i^{t+\Delta t}$ are obtained.

In the present work, we are developing an implicit formulation that involves the apparent viscosity term, its gradient, and deformation, utilizing previously calculated velocity, and the velocity Laplacian term, solved implicitly.

$$\mathbf{u}_i^* - \frac{\Delta t}{\rho}[\eta^t \langle\nabla^2 \mathbf{u}\rangle_i^*] = \mathbf{u}_i^t + \frac{\Delta t}{\rho}[2\mathbb{D}\nabla \cdot \eta^t + \rho\mathbf{f}]^t. \tag{14}$$

where $\mathbf{u}_i^t$ and η^t represent the velocity of particle i and the apparent viscosity calculated from the values obtained at the previous time step. In the present study, the term with the gradient of the apparent viscosity was disregarded.

3   Validation and tests

3.1   Flow between two parallel flat plates

This case examines the 2D flow between two parallel plates caused by a constant acceleration force acting parallel to the plates in the x-direction (left to right). The acceleration field's magnitude is determined by the momentum conservation equation. The geometry and boundary conditions of this setup is illustrated in Figure 2. The computational domain has the dimension of 0.2 x 0.5 m, no slip wall boundary condition was applied on the top and bottom boundaries, and periodic boundary conditions were applied at both left and right ends.
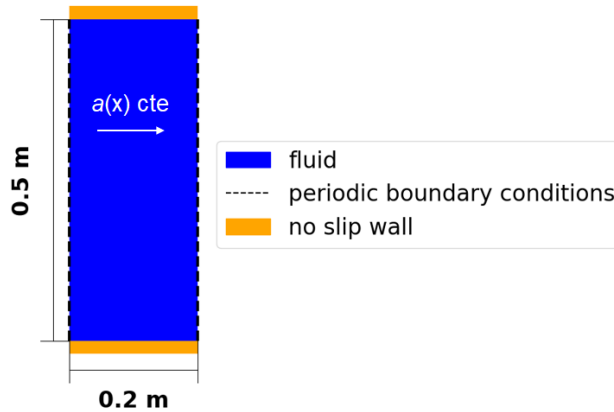
Figure 2: Geometry and boundary conditions of flow between two parallel plates.

Table 1. Validation tests

Acceleration a $\left[\frac{m}{s^2}\right]$	Bingham number
0.125	1.931
0.175	1.217
0.250	0.782
0.375	0.490

The velocity profile of the Bingham fluid flow between two parallel plates was obtained analytically by:

$$u(y) = \begin{cases} \frac{1}{2}\frac{dP}{dx}y^2 - \frac{1}{\eta}\left(\frac{h}{2}\frac{dP}{dx} + \tau_0\right)y, \ 0 \leq y \leq y_{lim} \\ u_{max} = -\frac{1}{2\eta}\frac{h^2}{4}\frac{dP}{dx} + h\tau_0 + \frac{\tau_0^2}{\frac{dP}{dx}}, \ y_{lim} \leq y \leq (h - y_{lim}) \\ \frac{1}{2}\frac{dP}{dx}(h-y)^2 - \frac{1}{\eta}\left(\frac{h}{2}\frac{dP}{dx} + \tau_0\right)(h-y), \ (h - y_{lim}) \leq y \leq h \end{cases} \quad (15)$$

In numerical simulations, we compared the analytical values with semi-implicit and implicit formulations, as well as the results obtained by [14]. The simulated Bingham fluid had a plastic viscosity of $50 \ Pa.s$, a density of $2200 \ kg/m^3$, and a yield stress of $15 \ Pa$. Table 1 shows the acceleration values a and corresponding Bingham numbers Bi. The numerical parameters adopted were a particle spacing of 5 mm, a time step of 2×10^{-6}s for [14] and the semi-implicit MPS and a time step of 5×10^{-4} for the implicit MPS, and a regularization parameter $m = 200$.

Figure 3 illustrates the velocity profiles of the Bingham fluid flow obtained by the four methods: analytic (orange dots), Mata et al. (green dots), semi-implicit MPS (blue dots), and implicit MPS (red dots). The results show that a higher Bingham number (Bi) is associated with higher yield stress, resulting in a smaller sheared region and a higher velocity gradient between the plates, and the implicit formulation closely matches the analytical solution for the fluid in a steady state.
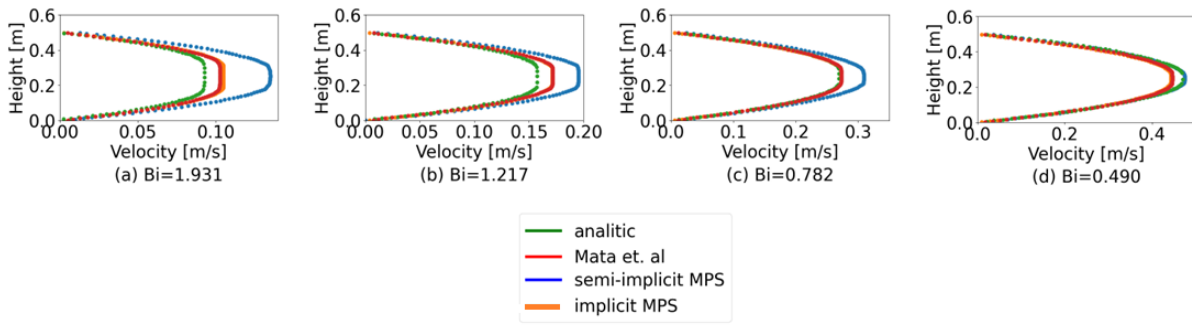
Figure 3: Velocity profiles obtained for a Bingham fluid with $\tau_0 = 15$ Pa at different Bingham numbers. The graphs show acceleration values of: (a) 0.125 m/s², (b) 0.175 m/s², (c) 0.250 m/s², and (d) 0.375 m/s.

Table 2: Processing time

Cases	Semi-implicit method	Implicit method
0.125 m/s^2	11h1min	25min
0.175 m/s^2	11h4min	17min
0.250m/s^2	11h2min	16min

Table 2 shows the processing times for the simulated cases using both the semi-implicit and implicit methods. Overall, the implicit method is significantly more efficient in terms of processing time compared to the semi-implicit method.

4   3DCP Simulations

The MPS simulations were conducted to model the extrusion of fresh mortar based on experiments by Comminal et al. [15]. The 3D model's geometry (Figure 3) includes an extrusion nozzle and a planar surface for concrete deposition. The nozzle is a cylindrical tube with a 25 mm inner diameter, and the planar surface has a predetermined motion, as adapted from the experiments.
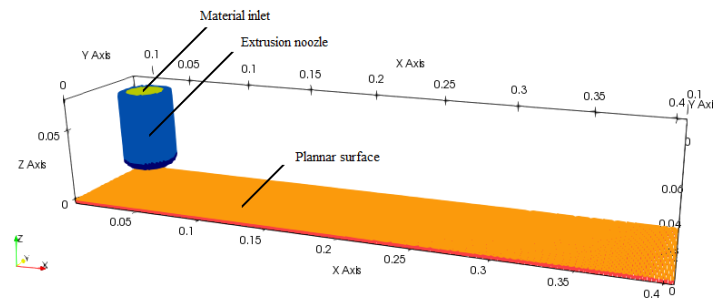
Figure 4: Geometry of the model.

The numerical investigation included simulations with varying printing speeds (V) and extrusion volumetric flux (U). For our parametric study, we modeled the relative movement between the nozzle and the table, where the table moves at speed V while the nozzle deposits material at a rate of U. The simulation starts with the nozzle empty of fluid due to the high yield stress and resulting thin shear layer, which would cause instabilities if the nozzle were full at the start. The nozzle height is 17.5 mm. Test 1 with printing speed of 20 mm/s and extrusion volumetric flux of 0.0336 m/s and test 2 with printing speed of 50 mm/s and extrusion volumetric flux of 0.0369 m/s. The rheological and physical parameters are listed in Table 3.

Table 3: Rheological parameters and physical properties

Parameters	Symbols	Numerical values
Density	ρ	2100 kg/m3
Yield stress	τ_0	630 Pa
Plastic viscosity	μ_p	7.5 Pa·s
Strain rate	$\dot{\gamma}$	$10^{-1}s^{-1}$
Papanastasiou m	m	200
Gravity	g	9.80665 m/s^2
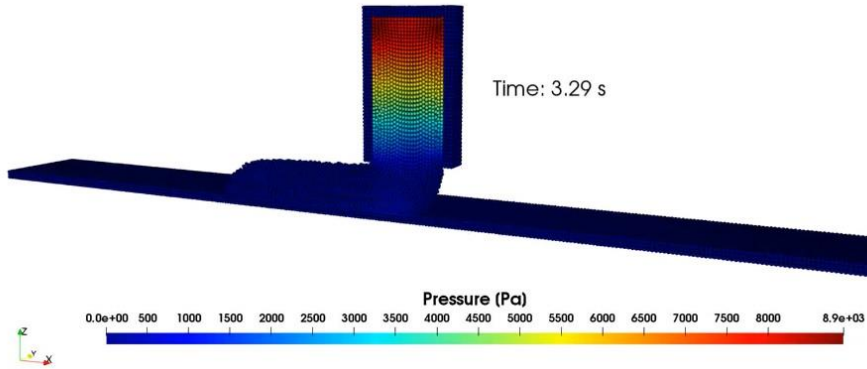
Figure 5: Snapshot of pressure profile in the implicit formulations with m=200, and $l_0 = 0.0025$m.

Figures 4 shows the pressure filed obtained by the implicit model. For the simulation of the implicit model, the time interval Δt is 5×10^{-4} s. The particle distance l_0 is 0.0025 m. The propagation velocity of the disturbances C_s is 5 m/s. The Papanastasiou regularization parameter (m) is 200. The total processing time is 3 hours.

The experimental results for the cross-sectional shapes from Comminal et al. [15] were measured at 50 cm from the initial deposition point of the concrete layer, using $l_0 = 0.00125$ m.

In Figure 5, comparisons are made between the cross-sectional shapes of the 2 tests conducted with the implicit formulation of the MPS and the numerical models EVP, GNF, and the experimental model by Comminal et al. (2020).
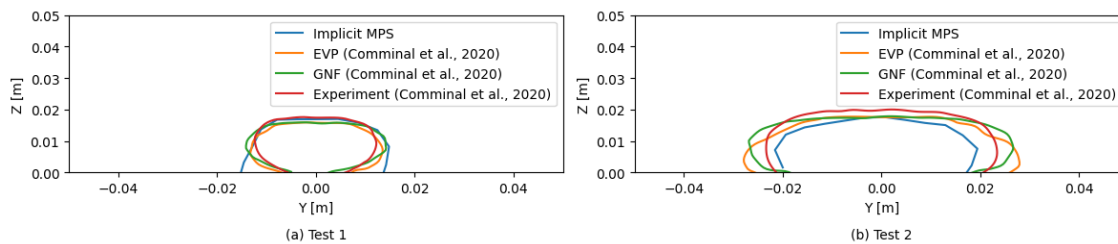
Figure 6: Cross-sectional shapes from the simulations and experiments.

Overall, the numerical and experimental results qualitatively agree well, with better alignment in test 1, which corresponds to the case with higher printing speed. As noted by Comminal et al. [15] the layer height tends to exceed the nozzle height, and this difference increases as the speed ratio V/U decreases. This phenomenon is observed only in test 1 of the MPS simulation, where the excess layer height is due to the limited space available to accommodate all the extruded material beneath the nozzle, resulting in an increase in layer height or width. However, further investigations are necessary to improve the implicit MPS model.

5   Conclusions

The simulations of non-Newtonian flow between parallel plates were validated against analytical solutions, showing satisfactory qualitative agreement. The implicit MPS formulation could replicate the velocity profile of Bingham fluids in a steady state. The 3D concrete printing simulations with varying printing speeds and extrusion volumetric fluxes demonstrated that the implicit method could predict the cross-sectional shapes of extruded layers Despite the promising results, the study observed that the printed layer height might exceed the nozzle height, particularly at higher printing speeds. This indicates the need for further investigations to improve the accuracy of the implicit MPS model, considering the spatial variability of apparent viscosity and extrusion dynamics. In conclusion, the implicit MPS method could be an effective tool for simulating 3D concrete printing, providing a better understanding of the dynamic behaviors during the extrusion process.

Authorship statement. The authors hereby confirm that they are the sole liable persons responsible for the authorship of this work, and that all material that has been herein included as part of the present paper is either the property (and authorship) of the authors or has the permission of the owners to be included here.

References

[1]   S. Lim, others, Developments in construction-scale additive manufacturing processes, Autom. Constr. 21 (2012) 262–268.

[2]   B. Zareiyan, B. Khoshnevis, Effects of interlocking on interlayer adhesion and strength of structures in 3D printing of concrete, Autom. Constr. 83 (2017) 212–221.

[3]   N. Ranjbar, others, Rheological characterization of 3D printable geopolymers, Cem. Concr. Res. 147 (2021). https://doi.org/10.1016/j.cemconres.2021.106498.

[4]   L. Reiter, T. Wangler, N. Roussel, R.J. Flatt, The role of early age structural build-up in digital fabrication with concrete, Cem. Concr. Res. 112 (2018) 86–95. https://doi.org/10.1016/j.cemconres.2018.05.011.

[5]   N. Roussel, Rheological requirements for printable concretes, Cem. Concr. Res. 112 (2018) 76–85. https://doi.org/10.1016/j.cemconres.2018.04.005.

[6]   W. Zhang, Y. Zhang, Apparatus for monitoring the resistivity of the hydration of cement cured at high temperature, Instrument. Sci. Technol. 45 (2016) 151–162.

[7]   R.J.M. Wolfs, F.P. Bos, T.A.M. Salet, Early age mechanical behaviour of 3D printed concrete: Numerical modelling and experimental testing, Cem Concr Res 106 (2018) 103–116. https://doi.org/10.1016/j.cemconres.2018.02.001.

[8]   A. Perrot, D. Rangeard, A. Pierre, Structural built-up of cement-based materials used for 3D-printing extrusion techniques, Mater. Struct. 49 (2015) 1213–1220.

[9]   T. Wangler, E. Lloret, L. Reiter, N. Hack, F. Gramazio, M. Kohler, others, Digital concrete: Opportunities and challenges, RILEM Tech. Lett. 1 (2016) 67–75. https://doi.org/10.21809/rilemtechlett.2016.16.

[10]   S. Koshizuka, Y. Oka, Moving-particle semi-implicit method for fragmentation of incompressible fluid, Nuclear Science and Engineering 123 (1996) 421–434.

[11]   T.C. Papanastasiou, Flows of materials with yield, J Rheol (N Y N Y) 31 (1987) 385–404.

[12]   L.Y. Cheng, R. Augusto Amaro Junior, E. Henrique Favero, Improving stability of moving particle semi-implicit method by source terms based on time-scale correction of particle-level impulses, Eng Anal Bound Elem 131 (2021) 118–145. https://doi.org/10.1016/j.enganabound.2021.06.018.

[13]   D. Morikawa, M. Asai, N. Idris, Y. Imoto, M. Isshiki, Improvements in highly viscous fluid simulation using a fully implicit SPH method, Comput Part Mech 6 (2019) 529–544.

[14]   M.S.D. Mata, F.K. Motezuki, L.Y. Cheng, F.A. Kurokawa, Modelagem numérica para fluidos não newtonianos utilizando o modelo bingham-papanastasiou e o método moving particle semi-implicit (MPS), in: Proc West Mark Ed Assoc Conf, 2017.

[15]   W.R. Comminal, T.J. da Silva, H. Andersen, J. Stang, Modelling of 3D concrete printing based on computational fluid dynamics, Cem. Concr. Res. 138 (2020). https://doi.org/10.1016/j.cemconres.2020.106256.